Investigation of transport processes across the sea surface microlayer by infrared imagery

U. Schimpf,[1] C. Garbe,[2] and B. Jähne[2]

Received 30 January 2003; revised 24 May 2004; accepted 15 July 2004; published 20 August 2004.

[1] Heat is used as a proxy tracer for gases to study the transport processes across the sea surface microlayer. Infrared imaging techniques permit fast measurements of heat transfer velocities and give an insight into the transport mechanisms across the thermal sublayer. The observed fluctuations of the sea surface temperature suggest that surface renewal is the major turbulent transport mechanism at medium and high wind speeds. The scale space analysis of the temperature patterns at the sea surface with respect to their contribution to the skin-bulk temperature difference shows the turbulent nature of the transport process. Large-scale turbulence dominates the transport at low friction velocities, whereas small-scale turbulence is more dominant at higher wind friction. The skin-bulk temperature difference is estimated by fitting the measured sea surface temperature distribution with a PDF function based on a surface renewal model. Periodic heat flux switching in the wind-wave flume delivers independent estimates of surface and bulk temperature and verifies the statistical approach, whereas at very low wind speeds and film-covered surfaces the statistical method underestimates the skin-bulk temperature difference across the thermal sublayer. The large scatter of the transfer velocities when plotted versus wind speed indicates that not only the wind shear but also other processes such as the wave field and surfactants influences near-surface turbulence and thus air-water gas transfer. *INDEX TERMS:* 4504 Oceanography: Physical: Air/sea interactions (0312); 4568 Oceanography: Physical: Turbulence, diffusion, and mixing processes; 4506 Oceanography: Physical: Capillary waves; 4594 Oceanography: Physical: Instruments and techniques; *KEYWORDS:* air-sea gas exchange, infrared imagery, turbulent transport

Citation: Schimpf, U., C. Garbe, and B. Jähne (2004), Investigation of transport processes across the sea surface microlayer by infrared imagery, *J. Geophys. Res.*, *109*, C08S13, doi:10.1029/2003JC001803.

1. Introduction

[2] The exchange of inert and weakly soluble gases including carbon dioxide, methane, and oxygen between atmosphere and ocean is governed by the interplay of turbulent transport and molecular diffusion in the 20–300 μm thick aqueous diffusive boundary layer, roughly one order of magnitude thinner than the thermal and viscous sublayer [*Jähne*, 1985]. Driven by the turbulent wind field, the friction at the water surface generates a shear current and turbulence in the sea surface microlayer and thus the transport of momentum, mass, and heat across the interface are closely related. For a smooth water surface, *Deacon* [1977] showed that the transfer velocity k is proportional to the water side friction velocity u_{*w}:

$$k = \frac{1}{\beta} u_{*w} Sc^{-2/3}, \tag{1}$$

where β is the dimensionless transfer resistance and the Schmidt number $Sc = \nu/D$ defines the ratio of the kinematic viscosity of water ν and D the diffusion coefficient of the dissolved gas in water.

[3] The complexity of the transport processes is caused by the wind blowing over the surface which not only causes a turbulent shear layer but also generates wind waves that interact with the turbulent shear layer and in turn influence the air flow. Moreover, short wind waves and near-surface turbulence are strongly influenced by traces of surface active material.

[4] It is well known that the turbulence very near the air-water interface is the key process which controls the rate of transfer of momentum, heat, and mass across the interface [*Jähne*, 1985]. Understanding of the key processes contributing to near-surface turbulence has increased considerably in the last decade [*Jähne and Haussecker*, 1989; *Jähne*, 1990; *Bock and Frew*, 1993; *Liss and Duce*, 1997]; nevertheless experimental techniques have only lately progressed to a state where direct measurements of relevant turbulence properties are feasible. Therefore parameterizations of the transfer velocity with environmental parameters are commonly used and, in particular, semiempirical parameterizations with wind speed are state-of-the-art and used for both modeling and global estimates of the carbon dioxide

[1]Institute of Environmental Physics, University of Heidelberg, Heidelberg, Germany.
[2]Interdisciplinary Center for Scientific Computing, University of Heidelberg, Heidelberg, Germany.

0148-0227/04/2003JC001803$09.00

uptake of the ocean [*Takahashi et al.*, 1997]. The two most popular relationships between transfer rate and wind speed were developed by *Liss and Merlivat* [1986] and *Wanninkhof* [1992].

[5] Currently, two conceptual theories for interfacial mass transfer exist. The small eddy model [*Coantic*, 1986], parameterizes the turbulent flux in the boundary layer with a local turbulent diffusion coefficient. The physical picture behind this approach is to describe the turbulent transport below the interface as a cascade of growing eddies. In contrast to the classical thin film model, it is found that the transfer coefficient k is proportional to the square root of the diffusion coefficient D.

[6] The surface renewal model is the second major concept reported in literature describing turbulent structures in the boundary layer. In addition to transport by molecular diffusion, small volume elements of the fluid are exchanged between the surface and the well mixed water bulk by eddies that penetrate into the boundary layer. The classical approach, postulated by *Higbie* [1935], assumed periodic time intervals in between two consecutive renewal events; later the exchange process was described by statistically or randomly occurring renewal events [*Danckwerts*, 1951], where the renewal frequency is related to the properties of the turbulence. Similar to the small eddy model, the surface renewal model predicts a proportionality of the transfer coefficient k to the square root of the diffusion coefficient D.

[7] Both the small eddy model and the surface renewal model predict the same Schmidt number exponent dependency of the transfer velocity [*Coantic*, 1986; *Csanady*, 1990], but differ significantly in their mean concentration profiles. In a review of various theories of mass transport across the air-sea interface, *Münsterer* [1996] stated that even multitracer mass balance experiments can only measure the dependence on crucial parameters (e.g., friction velocity, Schmidt number exponent, and surface roughness) that indicate when the transition from a solid wall to a free interface regime takes place. However, they cannot give any insight into the mechanisms controlling air-water transfer of momentum, mass, or heat.

[8] Nevertheless, experimental techniques capable of concentration profile measurements within the aqueous boundary layer allow the possibility to distinguish between the models. A quantitative analysis of concentration profiles obtained by laser-induced fluorescence (LIF) techniques revealed surface renewal structures in fluorescein images, where parts of the boundary layer were swapped into the bulk by larger eddies and showed that mean concentration profiles measured at wavy interfaces show better correspondence with the predictions of the surface renewal model than with those of the small eddy model [*Münsterer et al.*, 1995; *Münsterer and Jähne*, 1998].

[9] *Jessup et al.* [1997] reported signatures in the turbulent wake of breaking short wind waves without air entrainment, so-called microscale breakers, that can be detected by an infrared imaging technique. Breaking of waves disrupts the diffusive sublayer and *Csanady* [1990] has proposed that near-surface turbulence generated by microscale breaking waves is significantly controlling air-sea gas transfer. *Zappa et al.* [2001] have further shown that the fractional surface area coverage that is renewed by microscale breaking correlates with the gas transfer velocity.

[10] No experimental technique integrating over the water surface is able to distinguish between the two conceptual theories of air-water gas exchange. In order to assess the conceptual theories and to improve the transport models, new methods investigating gas exchange must fulfill two major requirements. Firstly, they have to be able to quantify all transport processes related to near-surface turbulence within the sea surface microlayer. Secondly, measurements of the transfer velocity have to be performed with sufficiently high temporal and spatial resolution to be compatible with the temporal and spatial variability of the underlying transport processes and forcing parameters.

[11] Lately developed infrared imaging techniques are a new and promising tool the meet the requirements mentioned above and have found widespread acceptance in recent years to visualize and to quantify processes controlling air-sea gas exchange [*Haussecker et al.*, 1995; *Jessup et al.*, 1997; *Jähne and Haussecker*, 1998; *Schimpf et al.*, 1999a; *Woolf and Ward*, 1999; *Veron and Melville*, 2001; *Zappa et al.*, 2001; *Garbe et al.*, 2002; *Haussecker et al.*, 2002].

[12] In this paper the basic concepts of using heat as a proxy tracer for gases to investigate the transport processes across the sea surface microlayer are presented and the previous work is reviewed (section 2). Utilizing digital imaging processing techniques, a quantitative investigation of the scale dependence of the microturbulence close to the interface has been carried out in the Heidelberg wind-wave facility. It is shown that the temperature fluctuations at the water surface are directly related to the skin-bulk temperature difference across the thermal sublayer and the observed surface renewal structures are reported (section 3). The two different conceptual methods for deriving the skin-bulk temperature difference in the laboratory and the field are described in section 4. Fitting of the sea surface temperature distribution based on surface renewal type of transport processes is applied to estimate the skin-bulk temperature difference in the field and verified in the laboratory. In section 5, the obtained transfer velocities are discussed in conjunction with the theoretical approaches describing air-sea gas exchange and the commonly used environmental parameterizations of the transfer rate with wind speed.

2. Heat as a Suitable Tracer for Investigating Transport Processes

[13] Typical mass balance methods are based on measuring the water side change of concentration of a tracer. It is distinguished between geochemical tracers (e.g., bomb-^{14}C [*Broecker et al.*, 1985], ^{222}Rn/^{226}Ra [*Kromer and Roether*, 1983]), or purposefully injected tracers (e.g., SF_6 [Wanninkhof, 1985]). The resulting mass flux density j across the interface is given by mass balance of the tracer concentration in the water volume V_W according to $V_w\dot{c}_w = F_w j$, where F_w denotes surface area of the water and $\dot{c}_w$ the change of concentration of the tracer. The resulting transfer velocity, k_{gas}, is given by the ratio of the flux density j and the concentration difference Δc across the boundary layer:

$$k_{gas} = \frac{j_{gas}}{\Delta c}. \tag{2}$$

[14] A major drawback of conventional mass balance methods is the dispersion of a tracer. The development of the dual tracer method [e.g., *Watson et al.*, 1991; *Wanninkhof et al.*, 1993] had the tremendous advantage of making it possible to correct for the dilution effect due to dispersion. However, the response time is of the order of hours to days, making a parameterization of the transfer velocity with parameters fluctuating on shorter timescales such as the wave field, wind forcing and surface chemical enrichments, nearly impossible (for a detailed discussion see [*Jähne et al.*, 1989; *Jähne and Haussecker*, 1998]).

[15] To overcome the disadvantages of conventional mass balance methods, *Jähne et al.* [1989] presented a completely different approach with the so-called controlled flux method. Instead of changing the concentration difference of a certain species and determining the transfer velocity from the measured flux density of the species, the procedure is inverted: a tracer flux is forced onto the water surface and the concentration difference is measured. In the first experimental setup of the controlled flux method, *Jähne et al.* [1989] forced a periodical heat flux density onto the water surface using chopped infrared radiation. The temperature response of the heated area at the water surface was detected with a point measuring radiometer and the characteristic timescale, $t_\star$, $\mathcal{O}(s)$, of the heat transfer process is calculated. According to *Jähne et al.* [1987], the local heat transfer coefficient, k_{heat}, is given by the molecular diffusion coefficient for heat in water, D_{heat}, and the characteristic timescale of the transfer process, $t_\star$, by the expression:

$$k_{heat} = \sqrt{\frac{D_{heat}}{t_\star}}. \tag{3}$$

[16] It was found that this method can be used to measure the heat transfer velocity locally with a temporal resolution on the order of minutes. In a further development of this technique, *Haussecker et al.* [1995] used a state of the art infrared imager as an areal detector of the SST (sea surface temperature) and a CO_2 laser to heat up a small spot $\mathcal{O}$ (cm) at the water surface. This approach, commonly referred to as active thermography, was for the first time successfully deployed in the field during the CoOP experiment 1995 in the eastern Pacific Ocean. Using advanced digital image processing techniques to track the heated spot and to analyze the temporal decay, it was possible to estimate the time constant of the transfer process and subsequently the heat transfer rate according to equation (3). Later, *Haussecker* [1996] presented an approach referred to as passive thermography, capable of estimating the temperature difference ΔT across the thermal sublayer under natural heat flux conditions, as occurring at the ocean surface, without using any artificial heat source. Assuming a simple surface renewal model with depth-independent renewal rate [*Danckwerts*, 1970], the theoretical distribution of the SST is calculated, provided that the net heat flux at the water surface is known. Fitting this function to the measured distribution gives an estimate of the temperature difference across the thermal sublayer. The latent, sensible, and radiative heat fluxes cause the SST to deviate from the bulk temperature. The common case is a heat flux density directed upward from the water surface, which results in a lowering of the SST, usually referred to as the cool skin of the ocean [*Saunders*, 1967]. The skin-bulk temperature difference, ΔT, net heat flux density, j_{heat}, and the transfer velocity for heat, k_{heat}, are related by:

$$k_{heat} = \frac{j_{heat}}{\rho\, c_p\, \Delta T}, \tag{4}$$

where ρ is the density of water and c_p specific heat capacity of water at constant pressure. Estimates of the skin-bulk temperature difference by passive thermography allow the calculation of the heat transfer velocity if the net heat flux density is known using equation (4). Recent advances in digital image processing techniques [*Haussecker and Fleet*, 2000] made it possible for the first time to estimate the net surface heat flux directly by analyzing infrared image sequences of the water surface [*Garbe et al.*, 2002]. Consequently, all the required quantities to calculate the transfer velocity for heat can be derived with high temporal and spatial resolution from infrared image sequences of the water surface. Using heat as a proxy tracer for gases provides a unique tool for investigating air-sea gas exchange processes suitable for both laboratory and field studies.

[17] In order to compare the transport of momentum, mass and heat, knowledge of the dimensionless Schmidt number $Sc = \nu/D$ of the observed species and the Schmidt number exponent n (2/3 for a smooth surface, 1/2 for a wavy surface) is required. A compilation of Schmidt numbers and solubilities of different gases, various volatile tracers, momentum, and heat for different temperature ranges is give by *Jähne* [2002]. In the literature, the Schmidt number for heat is mostly referred to as the Prandtl number, $Pr = \nu/D_{heat}$, $D_{heat} = \lambda\rho c_p$, where λ is the heat conductivity of water.

[18] The physical concept that a gradient drives a flux, with the flux density proportional to the diffusion coefficient and the concentration gradient, applies to the transport of heat, momentum, and mass [*Jähne and Haussecker*, 1998]. Consequently, equation (1) is valid for the transport of mass, heat and momentum. Dividing equation (1) for different species, particularly for heat and mass, yields:

$$\frac{k_{gas}}{k_{heat}} = \left(\frac{Pr_{heat}}{Sc_{gas}}\right)^n. \tag{5}$$

[19] From this so-called Schmidt number scaling the transfer velocities of arbitrary gases, k_{gas}, can be calculated if the heat transfer velocities, k_{heat} is known. Equation (5) is used to compare transfer velocities of different tracer gases (due to different diffusivities) or to correct for measurements made in different temperature regimes. The transfer velocity is commonly normalized to a Schmidt number of $Sc = 600$, an equivalent to carbon dioxide at 20°C. Extrapolating heat to gas transfer velocities using equation (5) requires a detailed knowledge of Schmidt numbers (e.g., for heat in water: $Pr = 7.0$ at a temperature of 20°C) for different species over a wide temperature range. Despite the large differences in Schmidt numbers of heat and carbon dioxide in water, *Jähne et al.* [1989] have shown in laboratory experiments that if the Schmidt number exponent n is known with an accuracy better than ±0.02 and the uncertainty of the diffusion coefficient is less than 5%, the

extrapolation of the transfer rate is correct within an error of 10%. The crucial issue for scaling heat transfer rates, but also for extrapolating transfer rates of gases with different diffusivities, is the drop of the Schmidt number exponent n from 2/3 to 1/2 with the onset of wind waves [*Jähne et al.*, 1984], which induce additional momentum transfer via pressure forces. *Jähne et al.* [1987] was the first to propose a strong correlation between the gas transfer coefficient and the mean square slope of waves. If this transient point with the onset of waves in the Schmidt number exponent is not carefully chosen, the extrapolated transfer rates may be significantly underestimated. Generally, this is not an easy undertaking, since, for example, surface chemical enrichments have a strong influence on the mean square slope of short wind waves and the transfer rate [*Bock et al.*, 1999]. In this context, a detailed discussion of the relation between air-sea gas transfer rate, wind stress, small scale roughness, and surface films are given by *Frew et al.* [2004].

3. Spatial Scale of Microturbulence in the Thermal Sublayer

[20] The exchange of heat, mass and momentum across the air-sea interface is governed by the interplay of turbulent transport and molecular diffusion. In the air and the water bulk, turbulent transport is very effective on large scales, contributing several orders of magnitude more to the mixing process than molecular diffusion. Approaching the surface, the physical picture changes since turbulent motions cannot penetrate the interface and are attenuated by viscous damping. The decrease of turbulent transport near the surface leads to a diffusive sublayer in which molecular diffusion on small scales will exceed the effect of turbulent transport. Consequently, effective turbulent mixing implies a small concentration gradient in the bulk and a large concentration gradient approaching the interface, reflecting the fact that the diffusive sublayer provides the main resistance for the transport across the interface. The thickness of this layer depends on the diffusion coefficient and the intensity of the turbulent motion at the very near-surface and, on the water side, is roughly $\mathcal{O}(20-300\ \mu m)$ for gases, $\mathcal{O}(100\ \mu m-1\ mm)$ for heat, and $\mathcal{O}(0.5-5\ mm)$ for momentum.

[21] Because of the cool skin of the ocean, any turbulent process responsible for the mixing of water within the thermal sublayer causes temperature fluctuations on the water surface. Therefore the sea surface temperature fluctuations associated with the interaction of diffusive and turbulent transfer at the air-sea interface give an insight into the transport mechanisms and thus make quantitative measurements possible. The use of highly sensitive $\mathcal{O}(15-30\ mK)$ infrared cameras allows measuring remotely the water surface temperature and the temperature fluctuations $\mathcal{O}(0.1\ K)$, respectively.

[22] Surface renewal events were observed in infrared image sequences in a wide range of wind speeds, at different scales, and under varying surface conditions. Figure 1 shows a compilation of different types of renewed surface structures. The infrared detector was directed at the water surface at an incidence angle of 20° and the images were recorded with a frequency of 60 Hz. The image sequences in Figures 1a–1c were acquired during the Coastal Ocean Processes (CoOP) 1997 Experiment in the North Atlantic. The image size is roughly 60 cm × 60 cm. An example of a single surface renewal event is shown in Figure 1a, where a patch with a size $\mathcal{O}(8 \times 8)$ of the cool surface was replaced by warmer water from the bulk at a moderate wind speed of u_{10} = 3.6 m/s. A much larger renewed structure (Figure 1b) on the surface $\mathcal{O}(30\ cm \times 20\ cm)$ occurred at a low wind speed of about u_{10} = 2.4 m/s. Rain drops, which impact on the water surface and penetrate into the water bulk cause the smallest renewed scales at the water surface $\mathcal{O}(mm^2-cm^2)$ and were also observed in infrared image sequences (Figure 1c) at a wind speed of u_{10} = 2.0 m/s. The infrared signature of a gravity wave breaking in the surf zone (Figure 1d) was recorded at Scripps Pier, La Jolla, California, in June 1998, at a wind speed of about u_{10} = 5.8 m/s. Image size is about 2 m × 2 m, frequency of the imager and incidence angle as mentioned above. Because of the low emissivity of foam, the crest of the wave appears bright (warm) in the images. Behind the crest the thermal boundary layer is disrupted, indicating that a large region behind the wave becomes turbulent and is renewed by warmer bulk water. *Jessup et al.* [1997] made the same observations by looking simultaneously at video and infrared images of microscale breaking events of short wind waves and concluded that infrared imaging techniques are capable of providing all the required information to quantify the breaking process. The observation of surface renewal events under a wide range of conditions support the hypothesis that for moderate and high wind speeds surface renewal is the predominant turbulent transport mechanisms in the sea surface microlayer.

[23] For a better understanding of the sea surface temperature fluctuations and thus the microturbulence close to the interface, it is necessary to investigate the sea surface temperature distribution and the underlying renewal statistics. An analysis of the distribution of the SST allows the quantification of the statistical properties (e.g., probability distribution of the renewal time) of surface renewal processes [*Garbe et al.*, 2002]. Further insight into the transport processes across the thermal sublayer is gained by a scale analysis of the spatial temperature patterns at the ocean surface caused by near-surface turbulence. Here, a quantitative scale space decomposition of the infrared signatures of the water surface is presented.

[24] In a first step, the infrared images are convolved with an appropriate low-pass filter mask in the spatial domain to fulfill the sampling theorem and allow a subsampling of the image [*Jähne*, 1997]. By taking every other pixel in every other row and iteratively repeating the smoothing and subsampling, a multi grid data structure (Gaussian pyramid) in the spatial domain is formed. The resolution of the image decreases from level to level of the pyramid by a factor of two. Consequently, the Gaussian pyramid represents a series of low-pass-filtered images where only more and more coarse structures remain with increasing level. Afterward a band pass decomposition is achieved by subtracting the images of consecutive levels of the Gaussian pyramid [*Jähne*, 1997]. Since fine structures are progressively removed by the smoothing operation with increasing level, only certain scales of structures remain in each level of the resulting Laplacian pyramid. Because of subsampling, every level of the Laplacian pyramid spans an octave of wave numbers and scales respectively. The resulting struc-

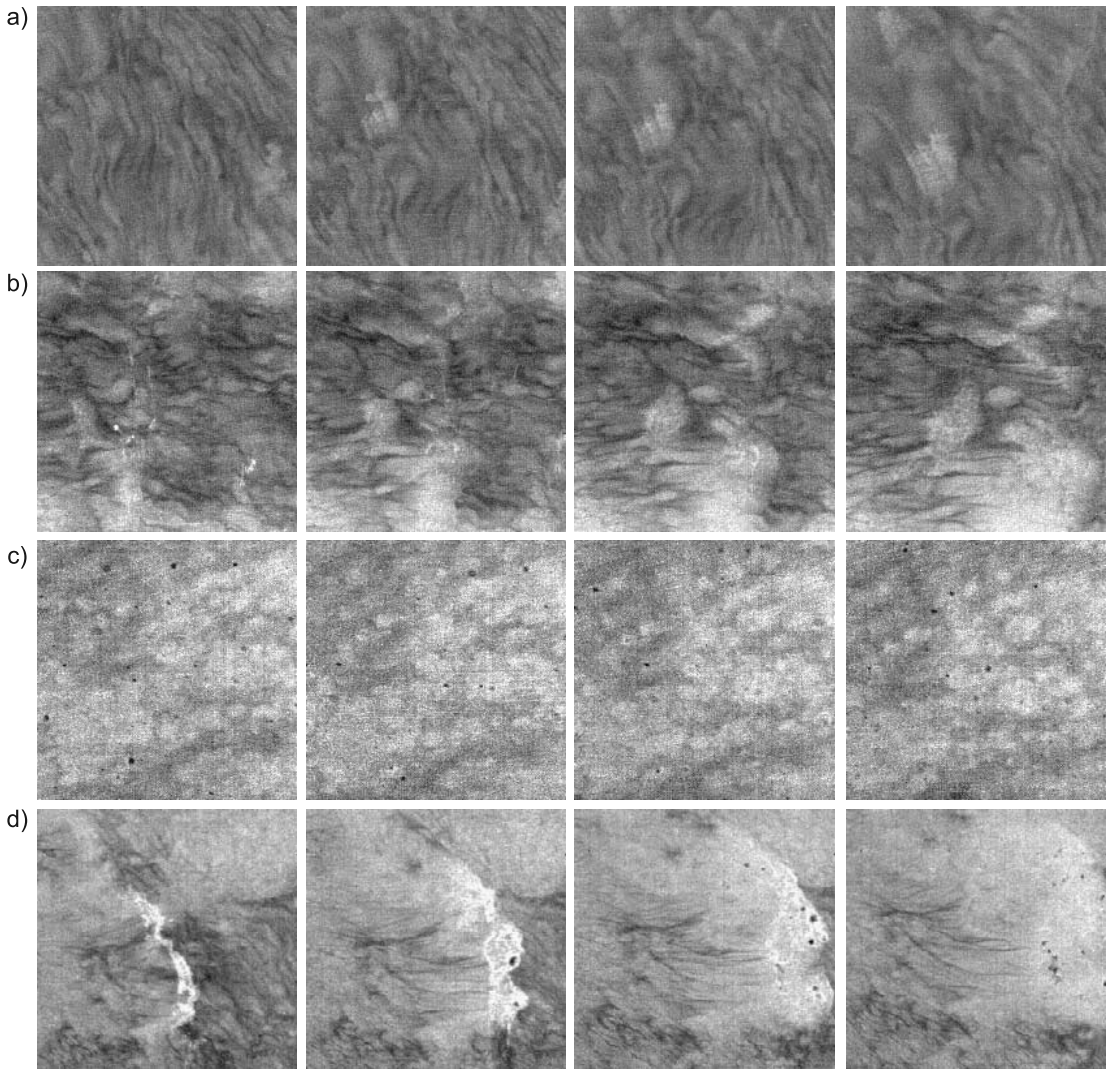

Figure 1. Infrared signatures of renewal structures at the ocean surface recorded during the Coastal Ocean Processes 1997 experiment in the North Atlantic. Image size: 60 cm × 60 cm, time between consecutive images: 0.0167 s. (a) Single small-scale renewal event, wind speed 3.6 m/s. (b) Single large-scale renewal event, wind speed 2.4 m/s. (c) Small-scale renewal events during rainfall, wind speed 2.0 m/s. (d) Turbulent wake of a breaking wave, image size 2 m × 2 m, recorded at Scripps Pier, La Jolla, California, in June 1998, at a wind speed of 5.8 m/s.

ture sizes for the different levels of the Laplacian pyramid are given in Table 1 for an image size of 20 × 20 cm during the measurements in the wind-wave facility.

[25] From each image sequence the Laplacian pyramid and the standard deviation of the temperature distribution at every level was computed. Because of this scheme of band pass decomposition, the standard deviation at each level is a measure for the presence of the corresponding spatial scale. A high value of the standard deviation corresponds to a high fluctuation in temperature for the appropriate structure size (see Table 1). The standard deviation at a given scale, divided by the skin-bulk temperature difference gives a measure for the contribution of this scale to the temperature difference and thus to the mixing process in the thermal sublayer.

[26] With increasing friction velocity at a clean interface, the presence of small scales (level 0: 0.22–0.44 cm) increases, the occurrence of large scales (level 4: 3.36–6.72 cm) decreases, and for medium scales (level 2: 0.84–1.68 cm) the standard deviation for all observed friction velocities is of the same order. At low friction velocities, large-scale turbulence contributes most (roughly 15–20%)

Table 1. Center Wave Numbers and Structure Sizes of the Different Levels of the Laplacian Pyramid (Image Size: 20 cm × 20 cm)

Pyramid Level	Center Wave Number, rad/m	Structure Size, m
0	2010	0.22–0.44
1	1005	0.44–0.84
2	503	0.84–1.68
3	251	1.68–3.36
4	125	3.36–6.72

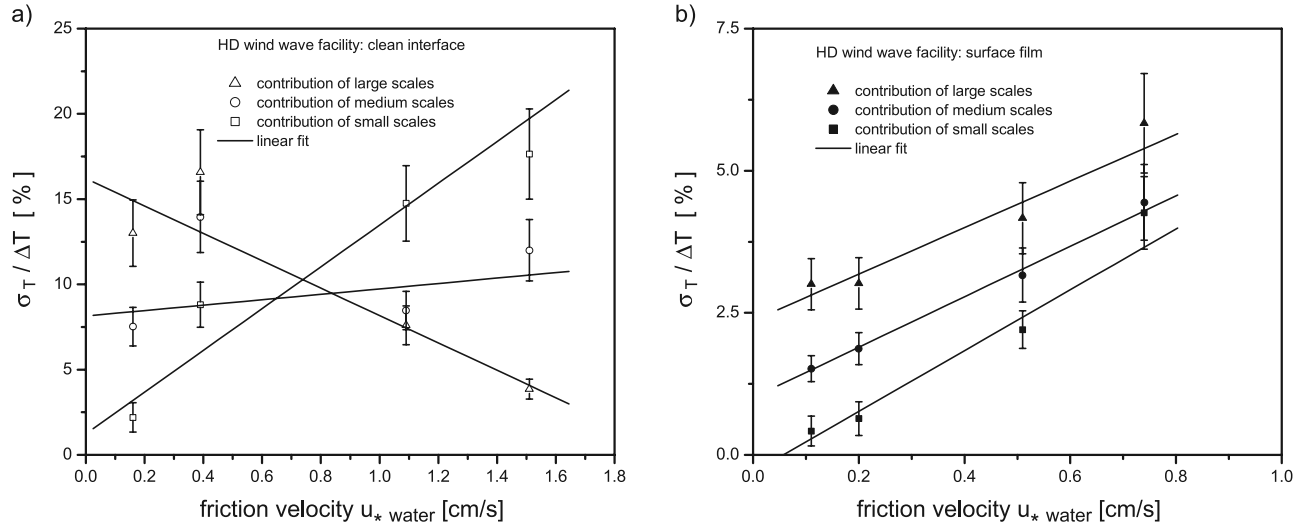

Figure 2. Contribution of small-, medium-, and large-scale turbulence to the temperature gradient across the thermal sublayer. The standard deviation of a certain scale (level 0, 2, and 4 of the Laplacian pyramid) of the temperature distribution is divided by the estimated skin-bulk temperature difference and plotted versus friction velocity (a) for a clean interface and (b) while a surfactant (Triton X-100, bulk concentration 3 ppm) was present.

to the mixing process in the thermal sublayer, whereas small-scale turbulence contributes much less (about 2–5%). The medium scales contribute equally (≈10%) in the observed friction velocity range to the mixing process. At a friction velocity of $u_\star \approx 0.8$ cm/s all scales contribute equally (about 10%) to the skin-bulk temperature difference (Figure 2a). Finally, at higher friction velocities ($u_\star \approx$ 1.6 cm/s) the smallest scales dominate the temperature distribution at the water surface and contribute most (about 20%) to the transport process across the thermal sublayer in comparison to the large scales (about 5%).

[27] The presence of a surfactant suppresses near-surface turbulence, attenuates the mixing process within the thermal sublayer and leads to larger temperature gradients across the thermal sublayer (compare Table 2). At low friction velocities, the contribution of small-scale turbulence to the skin-bulk temperature difference is negligible, and the larger scales contribute only about 3% to the temperature difference. In contrast to a clean interface the contribution of large scales increases (up to 6%) at a friction velocity of $u_\star \approx 0.8$ cm/s and is still dominant over the contribution of small scales (roughly 3%), as shown in Figure 2b. Consequently, the presence of a surfactant strongly influences the velocity and size scales of near-surface turbulence in the thermal sublayer and tremendously effects the transport process such that the heat transfer velocity decreases (Figure 7).

[28] The microscale temperature fluctuations at the water surface reflect the characteristics of near-surface turbulence and are directly related to the temperature gradient across the thermal sublayer. Accordingly, the observed surface renewal structures (Figure 1) and the statistics of the temperature fluctuations at the water surface justify the theoretical approach of estimating the skin-bulk temperature difference based on the sea surface temperature distribution in conjunction with a surface renewal model.

4. Estimating the Skin-Bulk Temperature Difference Across the Thermal Sublayer

[29] Detailed laboratory studies of the temporal and spatial statistics of the sea surface temperature distribution at the water surface and the relation to the air-sea exchange process have been carried out in the circular wind-wave flume in Heidelberg (HD 2 [*Jähne*, 2002]) and during the CoOP 1997 experiment in the North Atlantic Ocean.

[30] With the controlled flux technique, *Jähne et al.* [1989] forced a periodic radiative heat flux onto the water

Table 2. Results of the Measurements in the Wind-Wave Facility[a]

Series	Wind Speed, m/s	u_{*w}, cm/s	ΔT (DMT), K	ΔT (Fit), K
A	1.2	0.16	0.044 ± 0.003	0.041 ± 0.004
C	2.2	0.39	0.026 ± 0.004	0.032 ± 0.003
B	4.6	1.09	0.032 ± 0.004	0.038 ± 0.003
D	5.8	1.51	0.028 ± 0.003	0.034 ± 0.003
I	1.3	0.11	0.230 ± 0.024	0.071 ± 0.007
K	2.2	0.20	0.177 ± 0.012	0.111 ± 0.016
J	4.5	0.51	0.103 ± 0.007	0.115 ± 0.015
L	6.1	0.74	0.054 ± 0.003	0.052 ± 0.004

[a]Series A–D, clean interface; and series I–L, surfactant present (Triton-X-100, bulk concentration 3 ppm). Comparison of ΔT estimates of the fitted temperature distribution and of the difference of the measured mean temperatures (DMT).

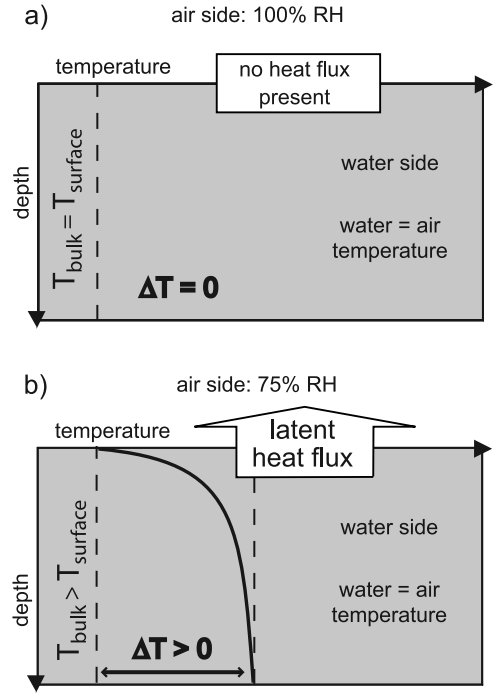

Figure 3. The two operating modes of the wind-wave facility: (a) water and air have the same temperature, relative humidity is ≈100%, no latent, sensible, or net radiative heat flux at the water surface is present. (b) Flushing the air space with dry air ($RH \approx 75\%$) creates an evaporative heat flux density that forces a skin-bulk temperature difference $\mathcal{O}(0.1\ \mathrm{K})$ across the thermal sublayer $\mathcal{O}(100\ \mu\mathrm{m} - 1\ \mathrm{mm})$.

surface with frequency $\mathcal{O}(\mathrm{s})$. Here, a different approach of employing the controlled flux technique was chosen: instead of a radiative heat flux, a latent heat flux was forced onto the water surface by controlling the humidity in the air space of the circular wind-wave tank. The relative humidity, *RH*, in the air space of the facility was held at a constant level ($RH = 75 \pm 5\%$) during the experiments by controlling the ventilation system (flushing rate: 1.5 m^3/min) of the gas tight facility (air space volume: 1.2 m^3) independently of the wind speed. If the ventilation system is shut down, the air temperature rapidly approaches to the water temperature because of the smaller heat capacity of the air. The relative humidity, *RH*, in the air space of the flume rises up to 100%, so that no latent, sensible, and radiative heat flux density at the water surface is present. This state of equilibrium is reached within a time period of $\mathcal{O}(1\ \mathrm{min})$. Flushing the air space of the flume with dry air of the same temperature as the water (maximum air-water temperature difference: ±1 K) leads to a decrease in humidity and creates an evaporative heat flux density, j_{lat}, at the water surface. According to equation (4), a net heat flux density forces a temperature gradient, ΔT, across the thermal sublayer. The two described modes of operating the wind-wave facility are illustrated in Figure 3.

[31] The flume is thermally insulated to prevent an additional sensible heat flux through the walls. The infrared camera used (Amber Galileo, Raytheon) is sensitive in the wavelength regime of 3–5 μm. Infrared radiation in this wavelength regime has a mean penetration depth in water of $\mathcal{O}(10\ \mu\mathrm{m})$ [*Downing and Williams*, 1975]. Thus the infrared imager is measuring the surface temperature of the water since the thermal sublayer thickness is $\mathcal{O}(100\ \mu\mathrm{m} - 1\ \mathrm{mm})$.

[32] Experiments in the wind-wave facility were carried out at four different wind speed conditions (1.2/2.2/4.5 and 6.1 m/s). The infrared camera recorded every ten seconds image sequences with 64 images each. In order to calculate the mean temperature and the standard deviation, the image sequences were temperature calibrated. During the laboratory measurements and the CoOP 1997 experiment a temperature calibration box was used, which contains three different temperature standards with an extended aperture to cover the whole field of view of the imager. The geometrical arrangement of the calibration and reference bodies, together with a special IR-coating make the device almost behave like an ideal blackbody. With this setup a relative temperature calibration with an accuracy of 25 mK can be performed. A detailed description of the calibration procedure is given by *Schimpf et al.* [1999b]. During the GasEx 2001 experiment, a commercial device (differential blackbody 2004, SBIR) was utilized for temperature calibration, allowing a relative accuracy of 25 mK. A temperature calibration of the infrared imager was performed before and after each set of the measurements in the laboratory, as well as in the field. During that time period (45–90 min), no drift in the temperature signal of the imager was observed.

[33] Figure 4 shows the mean surface temperature and standard deviation over a time period of 45 minutes. The latent heat flux was periodically switched on and off for five cycles, lasting ten minutes each. If no net heat flux density at the water surface is present, the relative humidity is up to 100% and the infrared imager measures the bulk temperature. The standard deviation of the surface temperature is at the noise level of the infrared camera ($\sigma_{noise} = 27$ mK) and no temperature fluctuations are present at the water surface. If the air space is flushed, an evaporative heat flux is created and immediately the surface temperature drops down a tenth of a degree. At the same time the standard deviation of the temperature increases and temperature fluctuations at the water surface are observed. The infrared imager detects the surface temperature. Accordingly, the skin-bulk temperature difference, is calculated from the mean bulk and mean surface temperature. This procedure was repeated for each wind speed condition. In four sets of measurements (referred to as A–D) the interface was clean, whereas in the following four sets (referred to as I–L), the experiments were repeated under the same wind speed conditions, but using a soluble surfactant (Triton-X-100, bulk concentration 3 ppm). A summary of the calculated mean values during each set of the experiment of temperature difference, wind speed, and water side friction velocity is given in Table 2.

[34] A different approach to estimate the skin-bulk temperature difference in the field is required, simply because it is not possible to control the heat flux densities at the ocean surface. The naturally occurring heat fluxes including latent, sensible, and radiative fluxes at the ocean surface cause the surface temperature to decrease or increase depending on the meteorological conditions. The net heat flux forces a temperature gradient across the thermal sublayer of $\Delta T = j_{heat}/(\rho\ c_p k_{heat})$ according to equation (4). Even if the natural occurring net heat flux is in the order of 25 Wm^{-2},

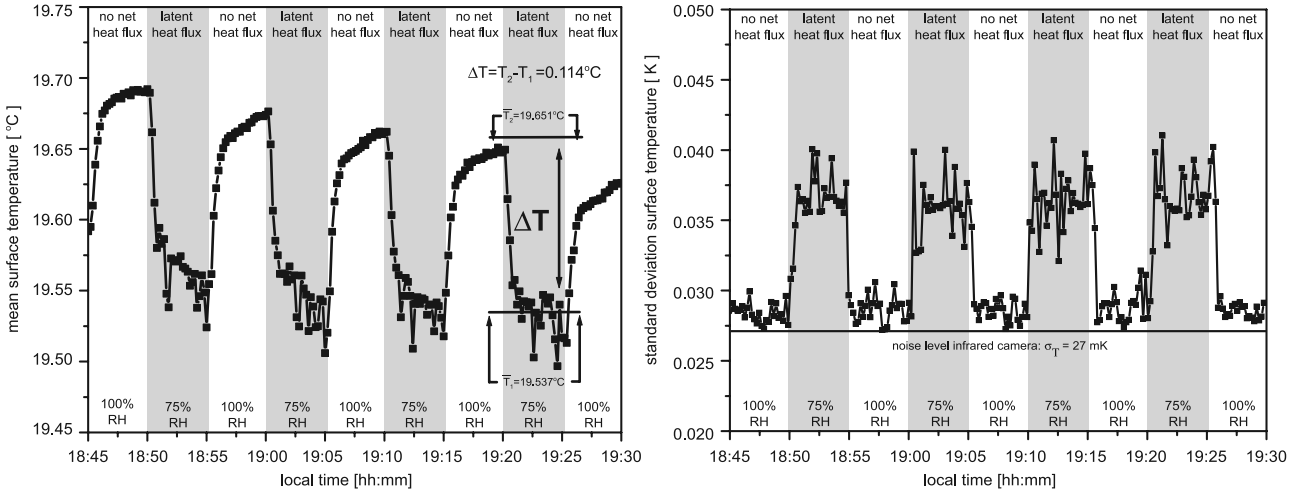

Figure 4. (left) Mean surface temperature and (right) standard deviation while the latent heat flux was periodically switched on and off (wind speed 4.5 m/s, slick-covered surface). If no net heat flux density at the water surface is present (relative humidity ≈100%, surface temperature fluctuations at noise level), the infrared imager measures the bulk temperature. Flushing the air space in the wind-wave facility creates an evaporative heat flux, the surface temperature immediately drops down, and temperature fluctuations at the water surface occur. The infrared imager detects the surface temperature. The skin-bulk temperature difference is calculated from the difference of the mean bulk and the mean surface temperature.

state-of-the-art, cryogenically cooled infrared cameras with high sensitivity are able to detect the resulting temperature fluctuations $\mathcal{O}(10-30$ mK) at the ocean surface.

[35] Assuming that surface renewal is the predominant turbulent transport process, *Haussecker* [1996] developed a statistical model to calculate the theoretical temperature distribution $h(T_s)$ at the ocean surface:

$$h(T_s) = \frac{2}{(\alpha j_h)^2}(T_s - T_b)\int_{t(T)}^{\infty}\frac{p(\tau)}{\tau}d\tau, \tag{6}$$

with $t(T) = [(T_s - T_b)/\alpha j_h]^2$ and where $p(\tau)$ denotes the probability distribution for the time in between two consecutive surface renewal events, T_b the bulk temperature, and $\alpha = 2(\rho\ c_p\sqrt{\pi D_h})^{-1}$. Fitting the measured distribution from calibrated infrared image sequences from the ocean surface with equation (6) delivers an estimate of the bulk temperature T_b. The difference of the expectation value of the SST, $\langle T_s\rangle$, which corresponds to the measured mean SST in the image sequences, and the bulk temperature, T_b, determines the skin-bulk temperature difference:

$$\Delta T = \left[\int T_s h^f(T_s)dT_s\right] - T_b = \langle T_s\rangle - T_b, \tag{7}$$

where $h^f(T_s)$ denotes the fitted temperature distribution.

[36] Assuming a classical surface renewal model and a lognormal probability distribution:

$$p(\tau) = \pi^{-0.5}(s\tau)^{-1}\exp\left(-\frac{(\ln\tau - m)^2}{s^2}\right), \tag{8}$$

for the time in between two consecutive surface renewal events the theoretical distribution, $h(T_s)$, is in good agreement with the measured sea surface temperature distributions [*Schimpf et al.*, 1999a].

[37] Figure 5 illustrates both available methods in the wind-wave facility to estimate the skin-bulk temperature difference. The left distribution of the surface temperature was obtained while a latent heat flux density was present (series J, wind speed 4.5 m/s, local time: 19:20–19:25; compare Figure 4), whereas the temperature distribution on the right hand side was calculated while no net heat flux density was present (series J, wind speed 4.5 m/s, local time: 19:15–19:20; see Figure 4). From the expectation values, $\langle T_s\rangle$ and $\langle T_b\rangle$, of both temperature distributions, the skin-bulk temperature difference is calculated. Additionally, the surface temperature distribution (while a net heat flux was present) was fitted with equation (6) and according to equation (7) the skin-bulk temperature difference, ΔT, estimated. The results delivered by the fit are in good agreement with the results from calculating the difference of the mean temperatures of both temperature distributions. In Table 2 the results of both methods are compared for all sets of the experiment in the wind-wave facility.

[38] In the case of a clean interface (series A–D), the estimates of ΔT agree very well within the errors for all occurring wind speeds supporting the hypothesis that surface renewal is the predominant turbulent transport mechanism. This is consistent with visual observations of surface renewal events (Figure 1) made in the field as well as in the laboratory. In presence of a surface film (series I–L) and low wind speed (series I: 1.1 m/s and K: 2.2 m/s) near-surface turbulence is dampened. Presumably, surface renewal type processes are no longer the dominant transport mechanisms and thus the fit of the measured temperature distribution with equation (6) underestimates the skin-bulk temperature difference for the series I and K. As the wind speed is increasing, the estimates of ΔT agree again within the error with the results of the difference of the

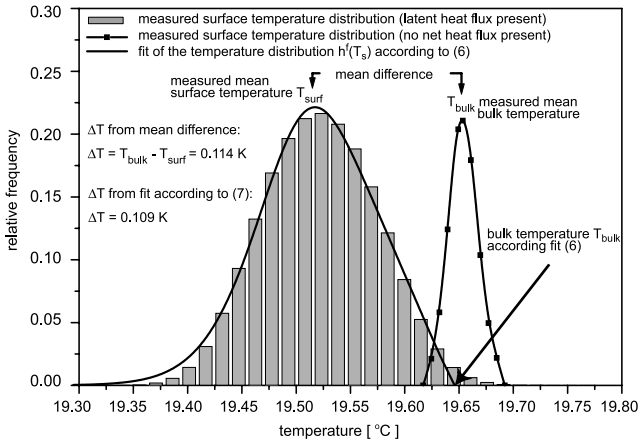

Figure 5. Left temperature distribution: latent heat flux density present, local time: 19:20–19:25. Right temperature distribution: no net heat flux density present, local time: 19:15–19:20. Wind speed: 4.5 m/s, slick-covered surface. The skin-bulk temperature difference is calculated from the difference of the measured mean temperatures. The distribution on the left-hand side was fitted with equation (6), and according to equation (7) the temperature difference was estimated. The result delivered by the fit (ΔT = 0.109 K) agrees with the difference of the mean temperatures (ΔT = 0.114 K) of both distributions.

mean temperatures of both distributions (series J: 4.5 m/s and L: 6.1 m/s; see Table 2).

5. Transfer Rates in the Laboratory and the Field

[39] In order to estimate the transfer velocity for heat, k_{heat}, according to equation (4), the net heat flux density, j_{heat}, at the water surface and the temperature gradient, ΔT, across the thermal sublayer must be known. In the wind-wave facility the estimates of the skin-bulk temperature difference were obtained by calculating the difference of the mean temperatures during the two different modes of operating the facility (see section 4) and averaged over five periods (Table 2). Assuming that no sensible and radiative heat flux densities are present, the latent heat flux density, j_{lat}, at the water surface is given by the ratio of the temporal change of the heat quantity of the water bulk,

$$\frac{d}{dt}Q = m\,c\frac{d}{dt}T, \tag{9}$$

and the water surface area (A = 3.5 m^2) in the wind-wave facility:

$$j_{heat} = \frac{m\,c}{A}\frac{d}{dt}T_{bulk}, \tag{10}$$

where m = 872 kg is the mass of the water bulk, c = 4190 $\frac{\mathrm{J}}{\mathrm{kgK}}$ the specific heat capacity of water and $\frac{d}{dt}T$ denotes the temporal change of temperature of the water bulk. By linear regression the temporal change of the bulk temperature (measured with PT-100 sensors) is calculated for each of the two modes of operation as illustrated in Figure 3. In Figure 6 the linear regression of the mean temperature of the water bulk during one period of heat flux switching in the wind-wave facility is shown. The averaged net heat flux densities for each set of the experiment are listed in Table 3.

[40] The transfer coefficient for carbon dioxide was calculated on the basis of Schmidt number scaling according to equation (5), assuming a Prandtl number of Sc = 7 for heat and a Schmidt number of Sc = 600 for carbon dioxide. During the sets of the experiment where a surfactant (Triton-X-100, bulk concentration 3 ppm) was present (series I–L) and at low wind speeds while the interface was clean (series A and C) a Schmidt number exponent of n = 2/3 was used, since no waves were visually observed and the water surface was smooth. At high wind speeds and a clean interface (series B and D), capillary waves were present and n = 1/2 was chosen. A summary of the conditions (wind speed, water side friction velocity, heat and scaled gas transfer rates) during each set of the experiment in the wind-wave facility is given in Table 3.

[41] The statistical method described in section 4 to estimate the skin-bulk temperature difference was used in the field for the first time during the CoOP experiment in April/May 1995 aboard the R/V New Horizon in coastal waters off California and later on during the second CoOP experiment aboard the R/V *Oceanus* on the North Atlantic in June/July 1997. During both experiments micrometeorological measurements to obtain quantities of heat flux density, wind speed, and water side friction velocity were carried out by J. B. Edson (WHOI). The provided heat flux data was used to calculate the heat transfer velocities according to equation (4). The temporal resolution of the heat transfer rate was limited by the estimates of the heat flux measurements to a 15 minute average. During both

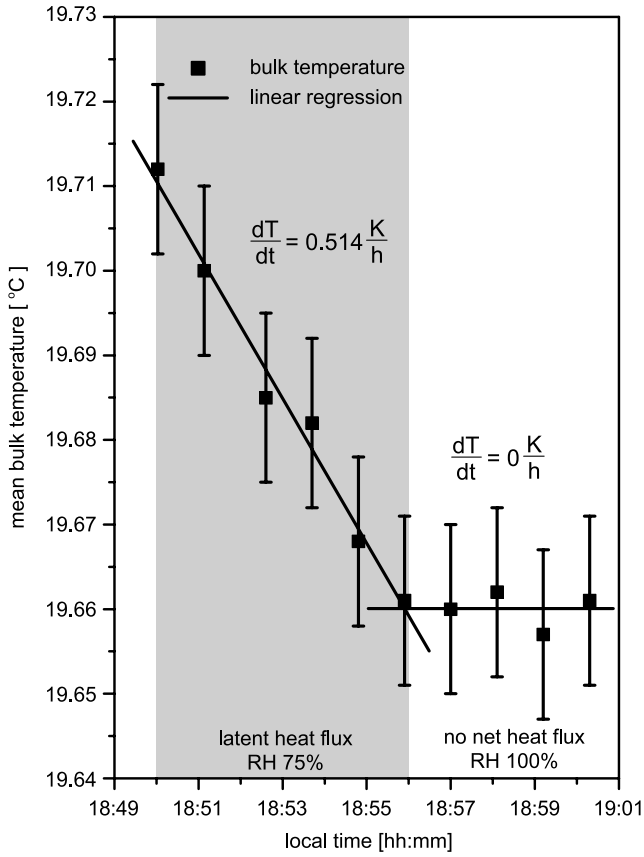

Figure 6. Mean temperature of the water bulk in the wind-wave facility during one period of heat flux switching.

Table 3. Results of the Measurements in the Wind-Wave Facility[a]

Series	Wind, m/s	$u_{\star w}$, cm/s	Heat Flux, W/m^2	$k_{Sc=7}$, cm/h	$k_{Sc=600}$, cm/h
A	1.2	0.16	−33.1	66.6 ± 6.4	3.42 ± 0.62
C	2.2	0.39	−25.7	89.4 ± 6.5	4.59 ± 0.66
B	4.6	1.09	−59.9	161.4 ± 6.8	8.31 ± 0.68
D	5.8	1.51	−67.7	217.6 ± 19.9	11.22 ± 2.21
I	1.3	0.11	−34.1	12.7 ± 1.5	0.66 ± 0.16
K	2.2	0.20	−32.9	15.4 ± 2.3	0.79 ± 0.24
J	4.5	0.51	−46.8	39.1 ± 5.1	2.01 ± 0.52
L	6.1	0.74	−39.6	62.9 ± 5.9	3.23 ± 0.61

[a]Series A–D: clean interface, series I–L: surfactant present (Triton-X-100, bulk concentration 3 ppm). Transfer velocity for heat using ΔT(DMT) values from Table 2 and scaled transfer velocity for carbon dioxide.

field campaigns the infrared camera recorded image sequences of eight images each every ten seconds for the duration of one hour. The image sequences were temperature calibrated (see section and the mean distribution of the sea surface temperature was calculated for a 15 minute average. The fit of the histogram with equation (6) delivered the skin-bulk temperature difference. The results of the experiments in the wind-wave facility showed that the fit delivers reasonable results for all data sets, except in presence of a surfactant at the water surface during low wind speed conditions $\mathcal{O}$(0–2 m/s).

[42] The heat transfer rates ($Sc = 7$) are calculated from the net heat flux and the skin-bulk temperature difference according to equation (4) and scaled to transfer coefficients of carbon dioxide ($Sc = 600$) using equation (5). Up to a wind speed of 3.6 m/s, which corresponds to a water side friction velocity of $u_{\star}w = 0.38$ cm/s, a Schmidt number exponent of $n = 2/3$ was used, for higher wind speeds $n = 1/2$. A summary of the results (wind speed, water side friction velocity, heat transfer velocity, and scaled transfer velocity) from the different field campaigns is given in Table 4.

[43] Recent advances in digital image processing techniques [e.g., *Haussecker and Fleet*, 2000] made it during the GasEx 2001 experiment in the equatorial Pacific for the first time possible to obtain estimates of the net surface heat flux directly by analyzing infrared image sequences of the water surface [*Garbe et al.*, 2002]. Furthermore, the temporal resolution of this method is only limited by the frame rate of the used infrared camera.

[44] In Figure 7 estimates of the heat transfer and scaled transfer velocities, obtained during the CoOP 1995 (data adapted from *Haussecker* [1996]), CoOP 1997, GasEx 2001 (first results from one deployment) experiments, and the results from the measurements in the Heidelberg wind-wave facility are plotted versus water side friction velocity.

[45] The results of the laboratory experiments are consistent with earlier measurements of *Jähne et al.* [1987] utilizing classical mass balance methods (*He*, CH_4, CO_2 and *Xe*) and a laser induced fluorescence technique [*Münsterer and Jähne*, 1998] employed in the same facility. At a slick-covered interface, near-surface turbulence is suppressed and thus the transport process across the interface is not as effective as in case of a clean interface. The presence of a surface film reduces the heat transfer velocity at constant wind stress roughly by a factor of five in comparison to a clean interface (see Table 3). Gas exchange experiments performed in the same wind-wave tank utilizing systematic variations of wind stress and surfactant concentration showed also a strong inverse relationship between gas transfer velocity and enhanced wave damping caused by a surface film [*Frew et al.*, 1995]. For a slick-covered interface, the transfer rates in the wind-wave facility are in good agreement with the theoretical approach of *Deacon* [1977]:

$$k = \frac{1}{15.2} Sc^{-0.61} u_{\star w} \quad \text{for} \quad 0.6 < Sc < 10 \tag{11}$$

$$k = \frac{1}{12.1} Sc^{-2/3} u_{\star w} \quad \text{for} \quad Sc > 60, \tag{12}$$

Table 4. Results of the CoOP 1995, 1997, and GasEx 2001 Field Campaigns

Experiment	Wind, m/s	$u_{\star w}$, cm/s	$k_{Sc=7}$, cm/h	$k_{Sc=600}$, cm/h
CoOP 1995	1.0	0.117	24.98 ± 9.07	2.69 ± 0.98
	3.5	0.432	47.86 ± 15.28	5.17 ± 1.65
	3.5	0.432	83.61 ± 16.94	9.03 ± 1.83
	4.5	0.563	65.08 ± 19.16	7.03 ± 2.07
	4.5	0.563	65.36 ± 27.16	7.06 ± 2.35
	6.0	0.778	86.01 ± 24.91	9.29 ± 2.69
	6.0	0.778	103.88 ± 28.89	11.22 ± 3.12
	9.0	1.232	191.92 ± 58.33	20.73 ± 6.30
	9.0	1.232	160.26 ± 46.94	17.31 ± 5.07
	9.0	1.232	207.01 ± 49.71	22.36 ± 5.37
	9.0	1.232	243.31 ± 60.36	26.28 ± 6.52
	9.5	1.313	141.84 ± 42.95	15.32 ± 4.64
	9.5	1.313	143.69 ± 44.72	15.52 ± 4.83
	11.5	1.642	203.22 ± 62.49	21.95 ± 6.75
	11.5	1.642	248.49 ± 64.07	26.84 ± 6.92
CoOP 1997	1.4	0.17	25.08 ± 4.63	1.29 ± 0.51
	2.1	0.24	32.66 ± 6.11	1.68 ± 0.66
	2.3	0.25	49.18 ± 12.04	2.53 ± 1.31
	2.4	0.27	41.21 ± 10.18	2.12 ± 1.09
	3.2	0.34	88.65 ± 9.26	4.56 ± 1.07
	3.6	0.38	41.48 ± 18.52	4.48 ± 2.03
	4.1	0.42	31.76 ± 15.74	3.43 ± 1.69
	4.3	0.44	47.68 ± 19.44	5.15 ± 2.1
	4.5	0.46	43.33 ± 10.74	4.68 ± 1.16
	4.9	0.50	52.31 ± 14.54	5.65 ± 1.57
	5.3	0.53	34.81 ± 14.81	3.76 ± 1.59
	5.6	0.56	71.19 ± 28.05	7.69 ± 3.03
	5.8	0.58	71.11 ± 27.13	7.68 ± 2.93
	6.2	0.61	88.23 ± 12.68	9.53 ± 1.37
	6.3	0.63	75.45 ± 30.37	8.15 ± 3.28
	6.7	0.66	89.90 ± 26.48	9.71 ± 2.86
	7.3	0.72	172.39 ± 22.43	18.62 ± 2.42
	7.6	0.75	158.04 ± 17.68	17.07 ± 1.91
	7.9	0.78	142.21 ± 13.98	15.36 ± 1.51
	8.2	0.80	157.48 ± 23.71	17.01 ± 2.56
	8.6	0.83	163.87 ± 7.78	17.71 ± 0.84
	8.8	0.85	164.89 ± 19.91	17.81 ± 2.15
GasEx 2001	4.8	0.608	111.78 ± 13.28	12.07 ± 1.23
	5.1	0.651	185.51 ± 21.48	20.04 ± 2.32
	5.3	0.678	151.89 ± 17.31	16.41 ± 1.87

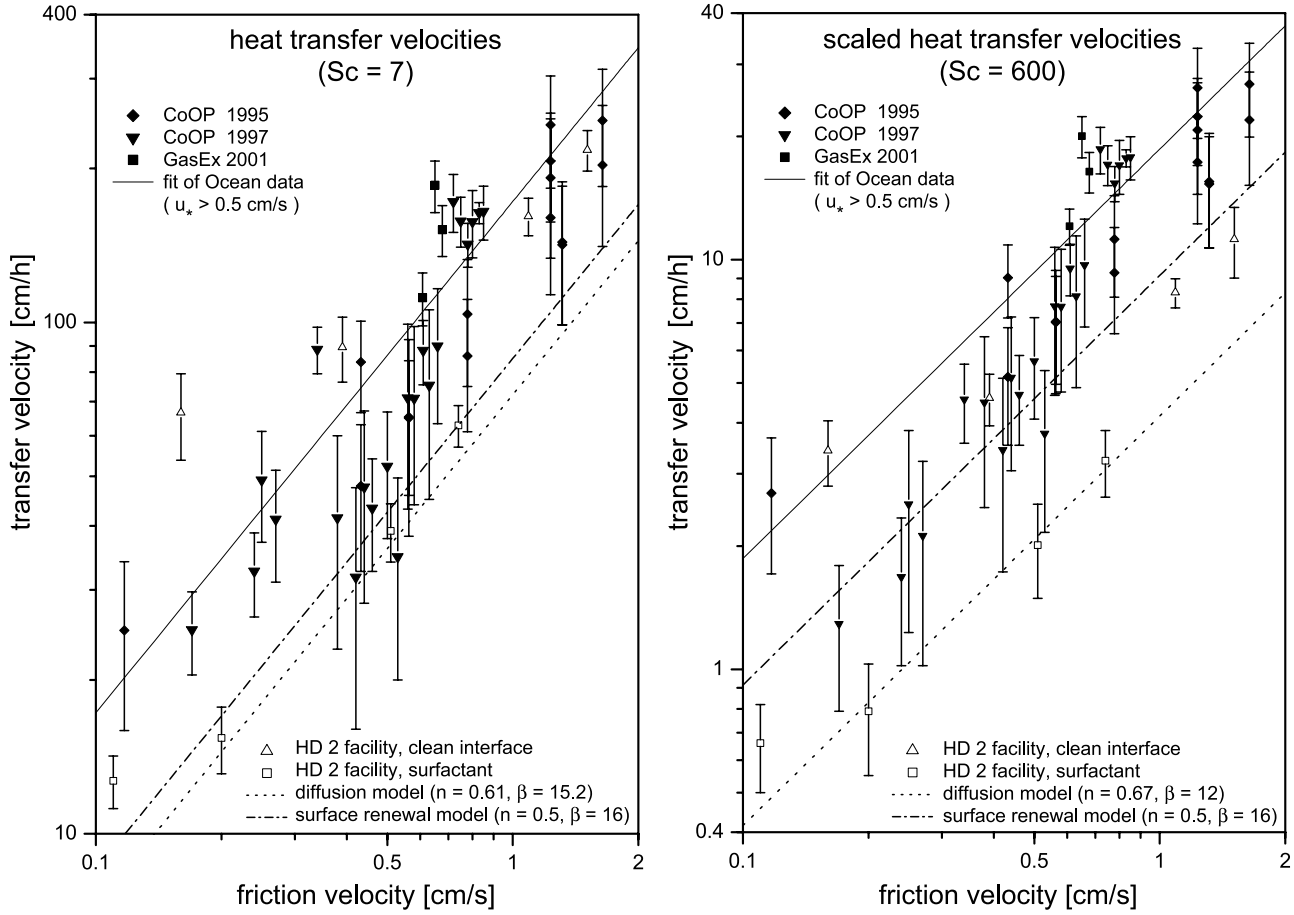

Figure 7. Heat transfer and scaled transfer velocities during the CoOP 1995, CoOP 1997, and GasEx 2001 experiments and in the wind-wave facility plotted versus water side friction velocity. For comparison the theoretical approaches of *Deacon* [1977], *Münnich and Flothmann* [1975], and a fit of the field data for $u_{\star}w > 0.5$ cm/s are shown.

based on a turbulent diffusion model using the constraint of a smooth surface. The term smooth refers to the fact that waves do not have an influence on the transport process, and is not used in a strict aerodynamical sense.

[46] For a clean interface in the wind-wave facility and thus in the presence of capillary waves the measured transfer rates are in agreement with the surface renewal model:

$$k = \frac{1}{16} u_{\star w} Sc^{-1/2}, \tag{13}$$

where the dimensionless transfer resistance $\beta = 16$ is estimated by a fit of the mean velocity profile of a turbulent flow near a smooth wall [*Münnich and Flothmann*, 1975].

[47] The transfer rates measured during the different field campaigns up to a friction velocity of $u_{\star}w \approx 0.5$ cm/s are close to the values predicted by the theoretical approach of *Münnich and Flothmann* [1975]. At higher friction velocities an offset in the transfer coefficient is observed. According to equation (1) a constant offset in the transfer velocity may be interpreted as a reduction of the dimensionless transfer resistance β, meaning an enhancement of turbulent transport. The theoretical approach of *Münnich and Flothmann* [1975] is based on a turbulent flow at a rigid wall and not on a wavy surface. The strong influence of short wind waves on the transport processes and the interaction with the turbulence driving the mixing process is supposedly the reason for the observed offset of the transfer velocities. A fit with

$$k = \frac{1}{\beta} u_{\star w} \ Sc^{-1/2} \tag{14}$$

for $u_{\star w} > 0.6$ cm/s of the transfer velocities measured in the field delivers yields a value of 7.9 for the dimensionless transfer resistance β.

[48] In Figure 8 the scaled transfer velocities ($Sc = 600$), obtained during the different field campaigns and in the wind-wave facility are plotted versus wind speed and compared with the empirical relationships of *Liss and Merlivat* [1986], *Wanninkhof* [1992], and *Wanninkhof and McGillis* [1999]. The presence of a surface film in the wind-wave facility significantly reduces the transfer coefficient. For the slicked case, the scaled transfer velocities are close to the first regime ($u_{10} < 3.6$ m/s) of the *Liss and Merlivat* [1986] relationship for a smooth surface: k [cm/h] = 0.17 u_{10} [m/s]. For a clean interface, the increase of the scaled transfer velocities with wind speed is nonlinear and the values for low wind speeds (1.2 and 2.2 m/s) are outside the area defined by the above mentioned relationships between wind speed and gas transfer rate. However, a comparison of the transfer rates measured in the wind-

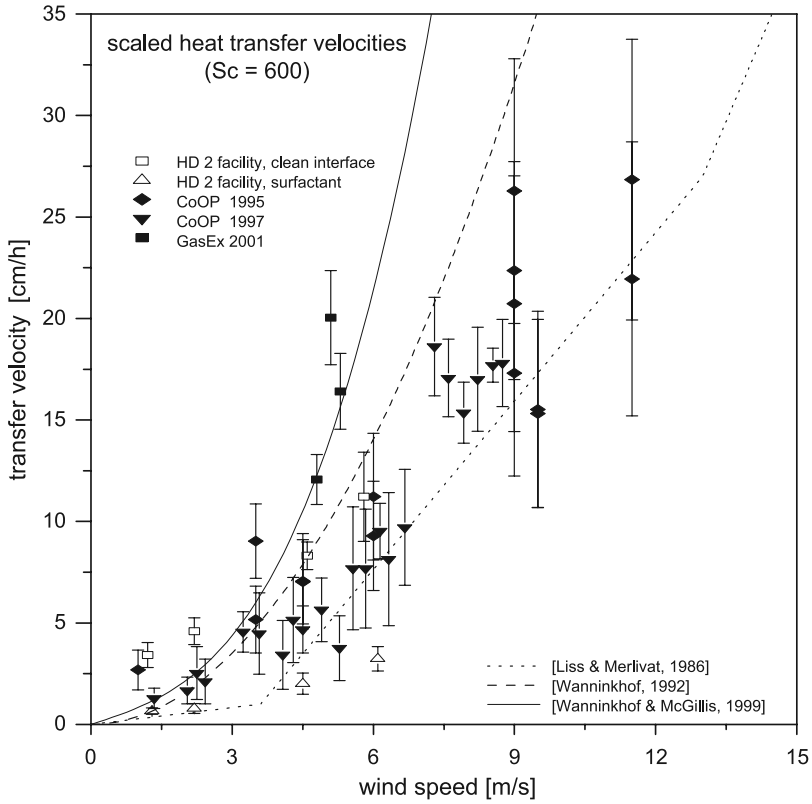

Figure 8. Scaled transfer velocities (k_{600}) during the CoOP 1995 (data adapted from *Haussecker* [1996]), CoOP 1997, and GasEx 2001 experiments and in the Heidelberg wind-wave facility plotted versus wind speed. For comparison the empirical relationships of *Liss and Merlivat* [1986], *Wanninkhof* [1992], and *Wanninkhof and McGillis* [1999] are shown.

wave facility with empirical relationships based on field experiments might not be appropriate, since the wind speed in the wind-wave facility is difficult to reconcile with the wind speed over the ocean at a given reference height of 10 meters.

[49] The observed wind speed dependence of the field derived transfer rates is nonlinear and fits roughly the above mentioned empirical gas exchange/wind speed relationships, but with considerable spreading. To a certain extent the scatter in the data is attributable to the variability of temporal and spatial fluctuations of the micrometeorological parameters, since estimates of wind speed and heat flux are limited to 15 minutes average. Nevertheless, the scatter in the transfer velocities indicates clearly that wind stress is not the only parameter influencing air-sea gas exchange, and other processes such as the wave field and surfactants significantly influence air-water gas transfer. For higher wind speeds the transfer rate is underestimated, since the applied method is insensitive to bubble mediated gas transfer due to the high solubility of heat in water.

[50] During the CoOP 1997 experiment, parameters of the wind-wave field, such as mean square slope and wave spectra of short wind waves, as well as surface chemical enrichments were also performed. For the CoOP 1997 data set it could demonstrated that the transfer velocity depends linear on the mean square slope of short wind waves (40–80 rad/m) and the relationship shows significantly less scatter than the parameterization of the transfer velocities with either wind speed or friction velocity [*Frew et al.*, 2004]. The high temporal and spatial resolution of the controlled flux technique provides for the first time the opportunity to perform measurements while traversing slicks. During the CoOP 1997 experiment, while entering a heavy banded slick the transfer velocity was significantly reduced and at the same time mean square slope of short wind waves dropped down in contrast to increasing ΔCDOM values [*Frew et al.*, 2004].

6. Concluding Remarks

[51] Observing the sea surface temperature by means of infrared imagery not only allows measurement of the heat transfer velocity at high spatial and temporal resolution but also gives an insight into the spatial structure of near-surface turbulence and thus the transport mechanisms in the thermal sublayer. The scale space analysis of the microscale temperature fluctuations at the sea surface shows the turbulent nature of the transport process across the thermal sublayer. At low friction velocities large-scale turbulence predominates the transport process, whereas with increasing wind friction a shift in the contributing scales occurs and eventually small-scale turbulence predominates at higher friction velocities. The results support the hypothesis that a surface renewal type of transport is the underlying turbulent transport mechanism of air-water gas exchange. Not only do the data fit the theoretical temperature distribution predicted by the surface renewal model, but also a wide range of surface renewed structures can be observed in infrared image

sequences of the water surface at different scales even under low wind speed conditions.

[52] For the laboratory studies it was found that periodical switching of the latent heat flux is a suitable method to estimate the skin-bulk temperature difference across the thermal sublayer. During the measurements the relative humidity was held at a constant level and the wind speed was varied. Although the effect of the relative humidity on the temperature gradient across the thermal sublayer appears implicitly, the final evidence that the relative humidity has no effect on the heat transfer rate cannot be supplied with this data set. Nevertheless, the measurements in the wind-wave facility showed that for clean interfaces at all wind speed ranges and for slick-covered surfaces at medium and high wind speeds, the skin-bulk temperature difference and thus the heat transfer rate is reliably determined by fitting the measured surface temperature distribution with a theoretical PDF function based on surface renewal. However, for low wind speeds and in presence of a surface film, surface renewal seems not to be the predominant transport mechanism and thus the theoretical approach underestimates the skin-bulk temperature difference.

[53] Both the measured transfer velocities in the wind-wave facility and during the field studies are consistent with measurements of other authors, allowing a discussion of the parameterization of air-water gas exchange in conjunction with the conceptual theories of mass transport across the air-sea interface. Despite the high temporal resolution of the applied technique the scatter of the transfer rates when plotted versus wind speed or friction velocity is still substantial and can only partly credited to fluctuations of the micrometeorological parameters. This clearly shows that wind friction is not the only significant parameter influencing air-sea gas exchange. Other processes such as the wave field, surface chemical enrichments, and bubble mediated transport have to be included in the parameterization. Using heat as a proxy tracer for gases in conjunction with other techniques might contribute to the understanding of air-water gas exchange in two ways. Firstly, the high temporal and spatial resolution of the method makes feasible a modeling of the transfer coefficient not only with wind forcing but also with additional parameters (e.g., mean square slope of short wind waves) influencing air-sea gas exchange. Secondly, the applied method is insensitive to bubble mediated gas transfer; that is, it measures the transfer rate of gases with high solubilities and thus coincident measurements of the transfer coefficient of gases might allow to distinguish and quantify the different mechanisms which contribute to air-water gas transfer.

[54] **Acknowledgments.** We thank J. B. Edson of Woods Hole Oceanographic (WHOI) for providing meteorological data during the Coastal Ocean Processes (CoOP) 1995 and 1997 experiments. We gratefully acknowledge financial support by the German Research Foundation (DFG), within the framework of the DFG Research Unit FOR240: Image Sequence Analysis to Investigate Dynamic Processes, the Office of Naval Research (ONR) and the National Science Foundation (NSF), within the Marine Boundary Layer (MBL), and Coastal Ocean Processes (CoOP) research initiatives, respectively.

References

Bock, E. J., and N. M. Frew (1993), Static and dynamic response of natural multicomponent oceanic surface films to compression and dilation: Laboratory and field Observations, *J. Geophys. Res.*, *98*, 14,599–14,617.

Bock, E. J., T. Hara, N. M. Frew, and W. R. McGillis (1999), Relationship between air-sea gas transfer and short wind waves, *J. Geophys. Res.*, *104*, 25,821–25,831.

Broecker, W. S., T. Peng, G. Östlund, and M. Stuiver (1985), The distribution of bomb radiocarbon in the ocean, *J. Geophys. Res.*, *90*, 6953–6970.

Coantic, M. (1986), A model of gas transfer across air-water interfaces with capillary waves, *J. Geophys. Res.*, *91*, 3925–3943.

Csanady, G. T. (1990), The role of breaking wavelets in air-sea transfer, *J. Geophys. Res.*, *95*, 749–759.

Danckwerts, P. V. (1951), Significance of liquid-film coefficients in gas absorption, *Ind. Eng. Chem.*, *43*, 1460–1467.

Danckwerts, P. V. (1970), *Gas-Liquid Reactions*, McGraw-Hill, New York.

Deacon, E. L. (1977), Gas transfer to and across an air-water interface, *Tellus*, *29*, 363–374.

Downing, H. D., and D. Williams (1975), Optical constants of water in the infrared, *J. Geophys. Res.*, *80*, 1656–1661.

Frew, N. M., E. J. Bock, W. R. McGillis, A. Karachintsev, T. Hara, T. Münsterer, and B. Jähne (1995), Variation of air-water gas transfer with wind stress and surface viscoelasticity, in *Air-Water Gas Transfer*, edited by B. Jähne and E. C. Monahan, pp. 529–541, AEON, Hanau, Germany.

Frew, N. M., et al. (2004), Air-sea gas transfer: Its dependence on wind stress, small-scale roughness, and surface films, *J. Geophys. Res.*, *109*, C08S17, doi:10.1029/2003JC002131, in press.

Garbe, C., B. Jähne, and H. Haussecker (2002), Measuring the sea surface heat flux and probability distribution of surface renewal events, in *Gas Transfer at Water Surfaces*, *Geophys. Monogr. Ser.*, vol. 127, edited by M. A. Donelan et al., pp. 109–114, AGU, Washington, D. C.

Haussecker, H. (1996), Measurements and simulation of small scale exchange processes at the ocean surface, Ph.D. thesis, Univ. of Heidelberg, Heidelberg, Germany.

Haussecker, H., and D. Fleet (2000), Computing optical flow with physical models of brightness variation, paper presented at Conference on Computer Vision and Pattern Recognition 2000, IEEE Comput. Soc., Hilton Head, S. C.

Haussecker, H., S. Reinelt, and B. Jähne (1995), Heat as a proxy tracer for gas exchange measurements in the field: Principle and technical realization, in *Air-Water Gas Transfer*, edited by B. Jähne and E. C. Monahan, pp. 405–413, AEON, Hanau, Germany.

Haussecker, H., U. Schimpf, C. Garbe, and B. Jähne (2002), Physics from IR image sequences: Quantitative analysis of transport models and parameters of air-sea gas transfer, in *Gas Transfer at Water Surfaces*, *Geophys. Monogr. Ser.*, vol. 127, edited by M. A. Donelan et al., pp. 103–108, AGU, Washington, D. C.

Higbie, R. (1935), The rate of absorption of a pure gas into a still liquid during short periods of exposure, *Trans. Am. Inst. Chem. Eng.*, *31*, 365–389.

Jähne, B. (1985), Transfer processes across the free water surface, Ph.D. diss., Univ. of Heidelberg, Heidelberg, Germany.

Jähne, B. (1990), New experimental results on the parameters influencing air-sea gas exchange, paper presented at Second International Symposium on Air-Water Mass Transfer, Am. Soc. of Civ. Eng., Minneapolis, Minn.

Jähne, B. (1997), *Practical Handbook on Image Processing for Scientific Applications*, CRC Press, Boca Raton, Fla.

Jähne, B. (2002), Air-sea interaction: Gas exchange, in *Encyclopedia of Ocean Sciences*, edited by J. Steele, S. Thorpe, and K. Turekian, pp. 122–131, Academic, San Diego, Calif.

Jähne, B., and H. Haussecker (1998), Air-Water gas exchange, *Annu. Rev. Fluid. Mech.*, *30*, 443–468.

Jähne, B., W. Huber, A. Dutzi, T. Wais, and J. Ilmberger (1984), Wind/wave-tunnel experiments on the Schmidt number and wave field dependence of air-water gas exchange, in *Gas Transfer at Water Surfaces*, edited by W. Brutsaert and G. H. Jirka, pp. 303–309, D. Reidel, Norwell, Mass.

Jähne, B., K. O. Münnich, R. Bösinger, A. Dutzi, W. Huber, and P. Libner (1987), On the parameters influencing air-water gas exchange, *J. Geophys. Res.*, *92*, 1937–1949.

Jähne, B., P. Libner, R. Fischer, T. Billen, and E. J. Plate (1989), Investigating the transfer processes across the free aqueous viscous boundary layer by the controlled flux method, *Tellus, Ser. B*, *41*, 177–195.

Jessup, A. T., C. J. Zappa, and H. H. Yeh (1997), Defining and quantifying microscale wave breaking with infrared imagery, *J. Geophys. Res.*, *102*, 23,145–23,153.

Kromer, B., and W. Roether (1983), Field measurements of air-sea gas exchange by the radon deficit method during JASIN (1978) and FGGE (1979), *J. Geophys. Res.*, *24*, 55–75.

Liss, P. S., and R. A. Duce (1997), *The Sea Surface and Global Change*, Cambridge Univ. Press, New York.

Liss, P. S., and L. Merlivat (1986), Air-sea gas exchange rates: Introduction and synthesis, in *The Role of Air Sea Exchange in Geochemical Cycling*, edited by P. Buat-Menard, pp. 113–127, D. Reidel, Norwell, Mass.

Münnich, K. O., and D. Flothmann (1975), Gas exchange in relation to other air-sea interaction phenomena, presented at SCOR Workshop on Air-Sea Interaction Phenomena, Miami, Fla.

Münsterer, T. (1996), LIF investigation of mechanisms controlling air-water mass transfer at a free interface, Ph.D. thesis, Univ. of Heidelberg, Heidelberg, Germany.

Münsterer, T., and B. Jähne (1998), LIF measurements of concentration profiles in the aqueous mass boundary layer, *Exp. Fluids*, *25*, 190–196.

Münsterer, T., H. J. Mayer, and B. Jähne (1995), Dual-tracer measurements of concentration profiles in the aqueous mass boundary layer, in *Air-Water Gas Transfer*, edited by B. Jähne and E. C. Monahan, pp. 637–648, AEON, Hanau, Germany.

Saunders, P. M. (1967), Aerial measurements of sea surface temperature in the infrared, *J. Geophys. Res.*, *72*, 4109–4117.

Schimpf, U., H. Haussecker, and B. Jähne (1999a), Studies of air-sea gas transfer and micro turbulence at the ocean surface using passive thermography, in *The Wind-Driven Air-Sea Interface*, edited by M. L. Banner, pp. 345–352, Univ. of New South Wales, Kensington, Aust.

Schimpf, U., H. Haussecker, and B. Jähne (1999b), Studies of small-scale air-sea interaction with active and passive thermography, in *Handbook of Computer Vision and Applications*, vol. 3, edited by B. Jähne, H. Haussecker, and P. Geissler, pp. 751–762, Academic, San Diego, Calif.

Takahashi, T., R. A. Feely, R. Weiss, R. Wanninkhof, D. W. Chipman, and S. C. Sutherland (1997), Global air-sea flux of CO_2: An estimate based on measurements of sea-air pCO_2 difference, *Proc. Natl. Acad. Sci.*, *94*, 8292–8299.

Veron, F., and W. K. Melville (2001), Experiments on the stability and transition of wind driven water surfaces, *J. Fluid Mech.*, *446*, 25–65.

Wanninkhof, R. (1992), Relationship between gas exchange and wind speed over the ocean, *J. Geophys. Res.*, *97*, 7373–7381.

Wanninkhof, R. W., and W. R. McGillis (1999), A cubic relationship between gas transfer and wind speed, *Geophys. Res. Lett.*, *26*, 1889–1893.

Wanninkhof, R. W., J. R. Ledwell, and W. S. Broecker (1985), Gas exchange-wind speed relation measured with sulfur hexafluoride on a lake, *Science*, *227*, 1224–1226.

Wanninkhof, R. W., W. E. Asher, H. Weppernig, P. Schlosser, and C. Langdon (1993), Gas transfer experiment on Georges Bank using two volatile deliberate tracers, *J. Geophys. Res.*, *98*, 20,237–20,248.

Watson, A. J., R. Upstill-Goddard, and P. Liss (1991), Air-sea exchange in rough and stormy seas, measured by a dual tracer technique, *Nature*, *349*, 145–147.

Woolf, D. K., and N. P. Ward (1999), The thermal signature of surfacing bubble plumes and air-sea gas exchange, in *The Wind-Driven Air-Sea Interface*, edited by M. L. Banner, pp. 273–274, Univ. of New South Wales, Kensington, Aust.

Zappa, C. J., W. E. Asher, and A. T. Jessup (2001), Microscale wave breaking and air-water gas transfer, *J. Geophys. Res.*, *106*, 9385–9391.

U. Schimpf, Institute of Environmental Physics, University of Heidelberg, Im Neuenheimer Feld 229, D-69120 Heidelberg, Germany. (uwe.schimpf@iwr.uni-heidelberg.de)

C. Garbe and B. Jähne, Interdisciplinary Center for Scientific Computing, University of Heidelberg, Im Neuenheimer Feld 368, D-69120 Heidelberg, Germany. (christoph.garbe@iwr.uni-heidelberg.de; bernd.jaehne@iwr.uni-heidelberg.de)